Non-filamentary (VMCO) memory: a two- and three-dimensional study on switching and failure modes

U. Celano[1], C. Gastaldi[1,2], S. Subhechha[1], B. Govoreanu[1], G. Donadio[1], A. Franquet[1], T. Ahmad[3], C. Detavernier[3], O. Richard[1], H. Bender[1], L. Goux[1], G. S. Kar[1], P. van der Heide[1] and W. Vandervorst[1,4]
[1]imec, Leuven, Belgium, email: umberto.celano@imec.be
[2] Polytechnic University of Turin, Turin, Italy, [3]University of Ghent, Ghent, Belgium, [4]KU Leuven, Leuven, Belgium

***Abstract*—** In this work, for the first time, a set of two- and three-dimensional (3D) analysis techniques are combined to clarify the nature of resistive switching (RS) in state-of-the-art TiO_2-based vacancy modulated conductive oxide (VMCO) memory. (1) A non-filamentary switching mechanism is observed. (2) The role of oxygen incorporation and motion in the TiO_2 is demonstrated. (3) The oxygen profile inside scaled cells is measured and a RS-model based on the modulation of oxygen inside the stack is proposed. In addition, we perform the tomographic analysis of fully-fabricated devices with Scalpel SPM, thus probing in 3D the entire stack and the contribution of TiO_2 grain boundaries (GBs) to the switching operations. Finally, devices failed by breakdown (BD) during cycling are characterized, identifying the formation of parasitic filaments as root-cause of the failure.

I. Introduction

Competing for the space of applications of storage class memory (SCM) and internet-of-things (IoT), VMCO have drawn the attention of the community as a self-rectifying, forming-free, low-power (<10µA) device with good endurance and high uniformity.[1], [2] Although to date the functionality of cells down to 40nm-size has been demonstrated, the direct experimental evidence of the switching mechanisms is still missing, due to the lack of suitable characterization techniques and challenging analysis conditions. Key issues such as on/off ratio, state retention, scalability and variability can be solved by improving our understanding on the physics of VMCO.

In this work, the combination of environmental Conductive Atomic Force Microscopy (C-AFM), Self-Focusing Secondary Ion Mass Spectrometry (SF-SIMS) and Scalpel SPM is used to unravel the switching mechanism in VMCO. First, the areal-type of RS is demonstrated for blanket films. Using a biased AFM tip, we unravel the role of oxygen in the switching operations by studying the impact of different environmental conditions, i.e. various O_2 and H_2O availability during cycling. Second, Scalpel SPM and SF-SIMS are combined to study fully-integrated cells (diameter Ø = 130 nm), identifying: (1) the 3D evolution of conductive channels and GBs in scaled devices, and (2) the formation of an oxygen-rich interlayer between (TiN/TiO_2). Based on our results, we relate the presence of interfacial oxygen with a defect modulated switching model in which changes of the oxygen profile inside the TiO_2 layer alter the resistance state. Finally, we observe the formation of parasitic (highly-conductive) filaments, in devices failed during cycling.

II. Results and Discussion

Fig. 1 shows the VMCO memory in our work, consisting of a bi-layer stack made of amorphous Si (a-Si) and TiO_2 that are sandwiched between TiN electrodes. The cell is fabricated starting from a 55-nm wide W plug following the steps listed in Fig. 1. The TiO_2 is grown by ALD and crystallize to anatase, while the TiN and a-Si are deposited using PVD. Fig. 2 shows the energy dispersive X-ray (EDS) elemental map of the stack where each layer is clearly visible. VMCO has an intrinsic current compliance induced by the stack, which allows to switch de memory element in a 0-Transistor/1-Resistor (0T1R) configuration using a low current (<10µA). In addition, the memory does not need a forming step, and shows a pristine low resistance state (LRS). Fig. 3 shows the I-V characteristics of a 45 x 45 nm^2 device in DC regime. A gradual reset at V_{reset} = 5 V increases the cell resistance by a factor ca. 10, in the high resistance state (HRS). Although TiO_2 is known to show valence change memory (VCM) switching, a clear area dependence is observed for the LRS of VMCO but not for VCM (Fig. 4), this indicates a different switching mechanisms for the two. Here we prepared two samples: (1) a bi-layer stack (TiO_2/a-Si) deposited as blanket thin film, where a biased AFM-tip is used to induce RS (Fig. 5a), and (2) an integrated cell (Fig. 5b) that is studied in 3D by SF-SIMS and Scalpel SPM.

A. Areal Switching (2D) and Defects Dynamics

Fig. 6a shows the morphology and the current map (C-AFM) of the TiO_2 surface. In here, the nanosized conductive tip acts as a virtual top electrode (TE) thus revealing the presence of distributed leakage paths. By scanning the biased tip with different polarity (table Fig. 6), LRS and HRS regions can be reversibly induced on the TiO_2 surface (Fig. 6b). Multiple densely packed conductive spots are visible in the LRS and recovered in the HRS, suggesting the absence of a single dominating filament for VMCO. Interestingly, also the prolonged tip-induced read-out (300 mV) can degrade the insulating properties of the TiO_2, as visible in the regions surrounding the switching regions (Fig. 6b after 10 cycles). Notably, once the LRS is induced, it tends spontaneously to drift in HRS. This process can be directly imaged as function of the time for the same region of space (Fig. 7a). Fig. 7b shows the evolution during ca. 6 min of the area and conductivity of

an individual cluster of conductive paths (dashed box in Fig. 7a) providing quantitate information. In other words, in an 'open system' such that constituted by the tip scanning on the TiO_2 surface, the HRS is energetically favored (inset Fig. 7b). However, by studying the progressive passivation of the defects constituting the LRS-cluster (Fig. 8a), we identify a monotonic current reduction that occurs around well-defined defective sites. The latter can be considered as the inner-structure of the percolative network that changes its conductivity reversibly by lateral growth or shrinkage induced by oxygen ions migration (Fig. 8b). Moreover, we observe how the tip-induced resistance states are affected by the C-AFM analysis conditions. Fig. 9 shows the dependency of the tip-induced resistive window (RW) while measuring in air, high vacuum (10^{-5} mbar) and UHV (10^{-10} mbar). It is worth to note that the capability to induce a detectable RW depends on the presence of oxygen. In UHV, once a LRS is induced this is not recoverable to HRS, while the opposite is observed in air (Fig. 7). This result clearly indicates the pivotal role of oxygen as the chemical species responsible for the RS also in VMCO.

B. Scalpel SPM Analysis (3D)

The understandings generated by C-AFM are complemented using Scalpel SPM and SF-SIMS in 3D on fully-integrated devices (Fig. 5b). These cells are fabricated by stopping the process after the formation of the TiN/Ru TE. As previously discussed, Ru is selected in view of its relatively easy removal by Scalpel SPM, while the 5 nm TiN guarantees the same electrical operations for this devices.[3] In this configuration, the TE is accessible by the AFM tip which is used to program the memory state and afterward for the slice-and-view analysis (Fig. 10). Fig. 11 shows the results of Scalpel SPM for two devices in a scan area 500 x 250 nm^2. More than 30 slices (i.e. C-AFM profiles) are acquired from the TE to the BE (ca. 35 nm height). Both cells are in LRS, in Fig. 11b each element of the stack (Fig. 11a) is visible as a set of 2D images acquired at different depths. Once the TE is removed, we access the area of interest i.e. the TiO_2, here the leakage paths their spots-size and density are directly probed (Fig. 12a). Consistently with our (*2D*) observation (Fig. 6), we do not observe a (single) dominant filament while multiple spots are visible on the active area. The table in Fig. 12 shows the details of spots carrying 10 nA and more, visible after the TE removal. Reducing the TiO_2 thickness by the progressive material removal, more spots become visible (Fig. 12b) due to the increased probability of leakage induced by trap-assisted- and direct-tunneling (Fig. 12c). A reconstructed 3D tomogram of the conductive channels inside the TiO_2 layer is presented in Fig. 13 (¼ of cell is shown in double cross-section). Interestingly, due to the presence of TiO_2 grains, the majority of the observed cells presented multiple GBs (ca. 4-5 nm width) appearing as regions of limited conduction. Fig. 14 shows two different cells after the TE removal in which GBs are clearly visible. In other words, inside the cell a network of lowly-conductive GBs exists and does not participate directly to the switching process. Due to their extension for the entire TiO_2 thickness, we can reconstruct this network in 3D as in Fig. 15.

C. Resistive Switching Mechanisms and Failure Analysis

Next we use SF-SIMS to determine the oxygen profile inside our stack. SF-SIMS allows to overcome the traditional spatial limitation of SIMS without sacrificing the sensitivity.[4] The concept is based on the ensemble analysis of cluster ions thus obtaining compositional information confined in a few tens of nm^3 albeit probing a large area. Fig. 16 shows the SF-SIMS profile acquired in a patterned area of 18 x 4 μm^2. The analysis of the TiO^- clusters shows the position of the TiO_2 layer in the stack, while the O^- profile indicates a clear oxygen accumulation at the TiN/TiO_2 (TE) interface, likely associated with the formation TiO_xN_y layer. In essence, Fig. 16 shows a profile representative for the pristine state as well as for the LRS, in which a non-uniform oxygen distribution is visible. In particular, the oxygen profile at the TE interface (Fig. 16b) combined with our previous observations allow us to propose a switching model in which a distributed (i.e. non-localized) modulation of the oxygen profile inside the stack occurs during the RS. Fig. 17 schematizes the different profiles for the two states. It is worth to mention that oxygen vacancies (Vös) in TiO_2 acts as donor, and the profile shown in Fig. 16b suggests that Vös accumulate at the TiN/TiO_2 interface, thus inducing a low-resistive pristine condition and LRS (Fig. 17a). On the contrary, the application of a positive polarity on the TE, redistributes the Vös in the TiO_2 leading to a relatively homogenous profile inside the layer, namely the HRS, as recently seen also for $SrTiO_3$.[5] Our previous observations on GBs, suggest that they are not altering the resistive state of the device. However, their contribution on physisorption and chemisorption of the migrating oxygen species cannot be excluded, likely introducing a source of variability and potential failure in ultra-scaled cells. Finally, we reverse engineer various failed devices, which are repeatedly cycled until breakdown (BD) occurs (Fig. 18a). The latter is a major type of failure often limiting the endurance of VMCO.[1,2] Fig. 18b presents the results using Scalpel SPM showing the appearance of a single conductive spot in such devices. Comparing our observation in Fig. 13, we can identify the root-cause of the failure after BD with the formation of a (single) highly conductive area in the TiO_2 leading to an unrecoverable LRS state of the cell.

III. CONCLUSIONS

In this work we elucidate the areal-switching mechanisms of VMCO, providing direct experimental evidences of a distributed, non-filamentary RS mechanism. Our results strongly indicate that the oxygen profile is modulated inside the TiO_2 for the two resistive states. The effective area involved in the RS is quantified, elucidating also the role of the GBs in TiO_2. Finally, the BD-induced failure is ascribed to the formation of unrecoverable localized filaments. Our observations increase our understanding on the VMCO operations thus enabling the next development towards low-current, high-density memory circuits.

[1] B. Govoreanu et al., in IEDM Tech. Dig., 2013, pp. 256–259.
[2] B. Govoreanu et al., VLSI Technol. (VLSIT), 2016 Symp., pp. 1-2
[3] U. Celano et al., Nano Lett., vol. 15, no. 12, pp. 7970–5, 2015.
[4] A. Franquet et al., Appl. Surf. Sci., vol. 365, pp. 143–152, 2016.
[5] D. Cooper et al., Adv., Mater., vol. 29, pp. 1700212, 2017

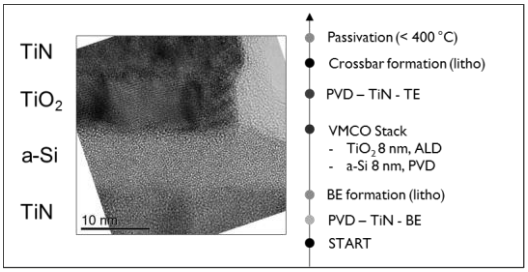

Fig. 1 High resolution TEM image of the VMCO stack used in this work, on the side the process steps for fabrication.

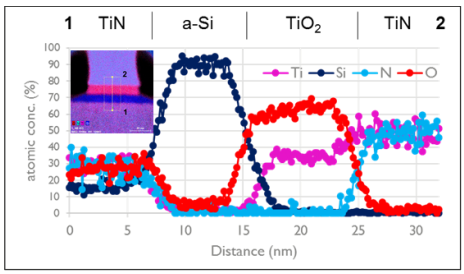

Fig. 2 EDS compositional profile of the VMCO stack acquired in the region 1-2 shown in the inset.

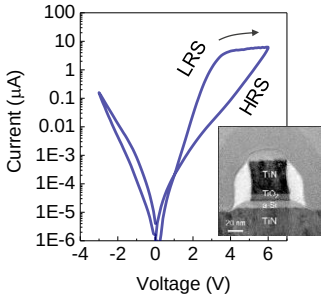

Fig. 3 I-V characteristic of a 45 x 45 nm^2 device, shown in the inset.

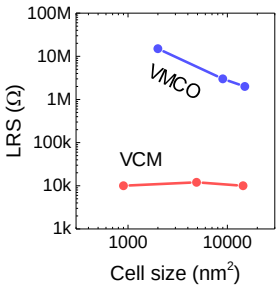

Fig. 4 LRS cell size dependency compared for VMCO and HfO_2-based VCM.

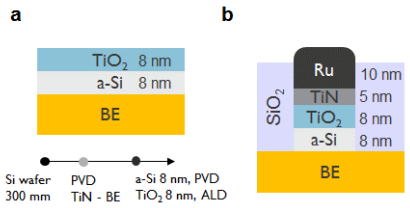

Fig. 5 (a) Schematic representation of the blanket sample used for the C-AFM analysis. (b) Schematic of the structure used for SF-SIMS and Scalpel SPM.

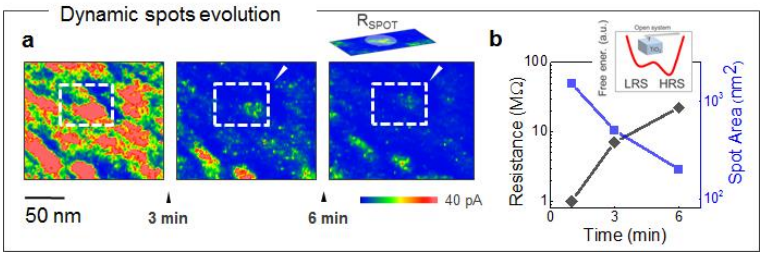

Fig. 7 (a) The transition of a region from the LRS to the HRS is dynamically probed over six minutes. As the LRS area progressively recovered to HRS a single cluster of spots can be investigated in details as in the 50 x 50 nm^2 box. (b) The evolution of resistance and spot-area are recorded simultaneously as function of the time.

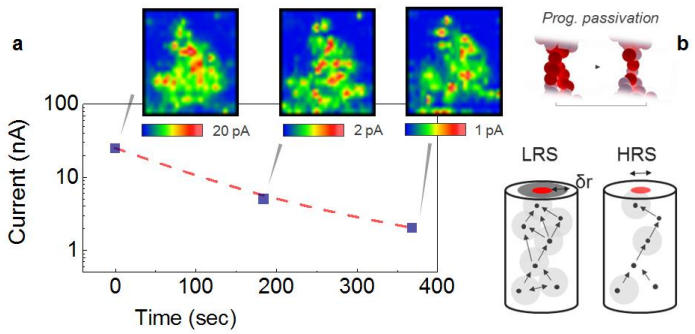

Fig. 8 The average current flowing in the 50 x 50 nm^2 area is shown combined with the current maps. A monotonic decrease of the average current is visible in the graph. For each data-point the current maps are shown using an adaptive data-scale that emphasizes the internal structure of the leakage path. Notably, the current reduction happens in correspondence of a few spots indicating an internal structure for the percolative path around pre-existing defective sites whose resistance is modulated. This process can be schematically seen in (b) alternating the lateral shrinkage and growth during the LRS-to-HRS transition and HRS-to-LRS respectively.

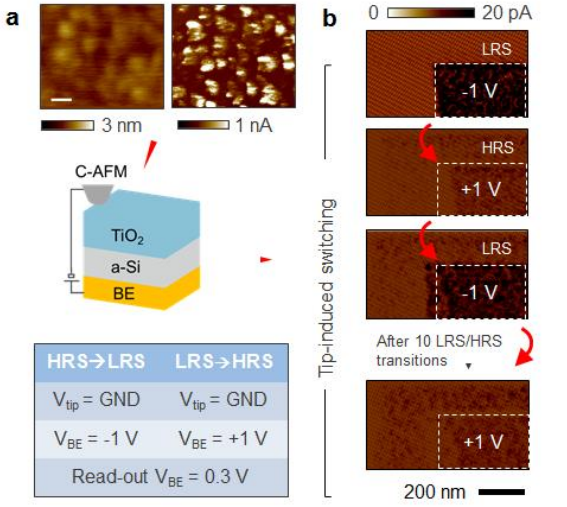

Fig. 6 (a) AFM morphology and current map of the TiO_2 surface (scale bar 50 nm). (b) RS is reversibly induced by the biased tip using the conditions reported in the table. Multiple read-out scans of the same area in LRS and HRS are shown. The areal-switching is clearly visible on the surface of TiO_2.

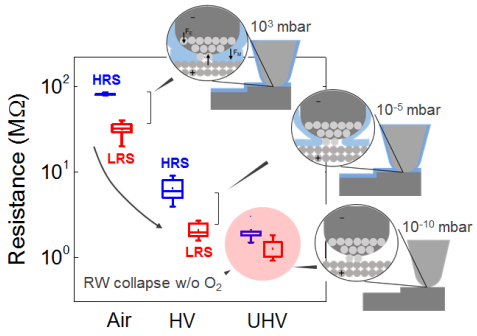

Fig. 9 Comparison of the RW induced by C-AFM working in different environments. In the inset, the AFM tips are shown in different humidity conditions with different level of absorbed moisture.

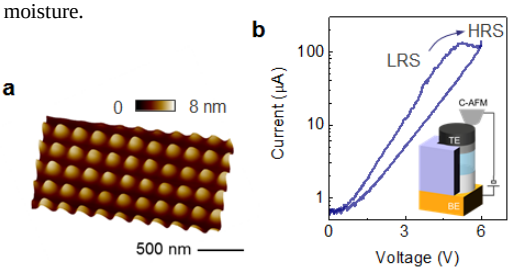

Fig. 10 (a) AFM image of the cells used for the measurement with Scalpel SPM, each dot represents an individual device. (b) The AFM tip is used to contact the TE and program the memory state.

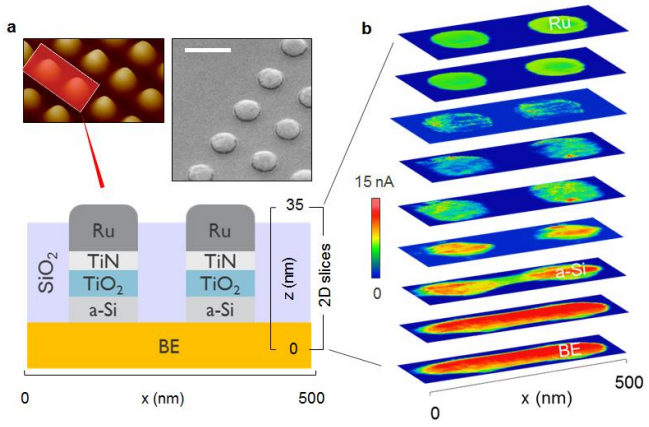

Fig. 11 (a) AFM and SEM of the dense array of cells fabricated for the 3D analysis. Scalpel SPM is performed on a 500 x 250 nm^2 area, containing two fully-fabricated devices as in the schematic (SEM scale bar 250 nm). (b) A portion of the 2D set (C-AFM profiles) constituting the entire stack is shown (total ca. 30 images). Note, from top to bottom all the parts of the stack are visible with their respective conductive map, clearly the area of major interest is represented by the TiO_2.

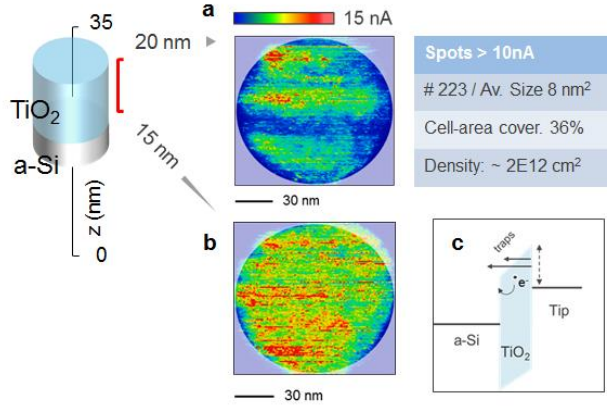

Fig. 12 Two individual C-AFM profiles of the TiO_2 are shown: (a) immediately after the top electrode is removed (ca. 8 nm thick TiO_2) and in (b) in proximity of the TiO_2/a-Si interface (ca. 3 nm thick TiO_2). In the table the quantitative information on the number of conductive spots carrying an electronic current > 10 nA is extracted: number, size and density are reported. In the inset the schematic description of the conduction mechanisms occurring (simultaneously) during the removal.

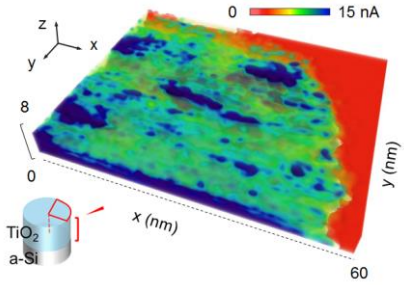

Fig. 13 Reconstructed 3D sectional view of the conductive paths in the TiO_2 (LRS). The image presents the 8 nm-thick TiO_2 layer. Multiple spots appear indicating the areal-switching mechanism.

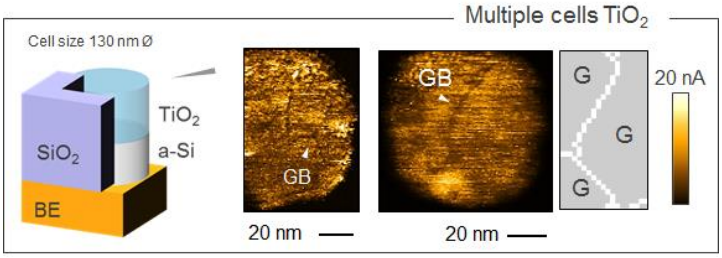

Fig. 14 Two current maps are shown for different devices after the top electrode is removed. The GBs are consistently observed in the TiO_2 creating a network of non-conductive regions within the active area of the device. Individual information on the probed GBs can be extracted.

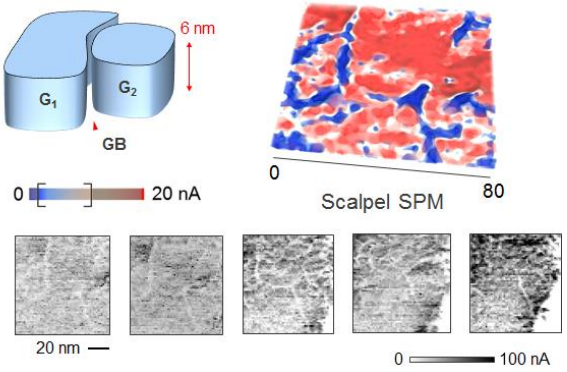

Fig. 15 After the top electrode is removed, GBs are consistently observed in the TiO_2 creating a network of non-conductive regions within the active area of the device, likely non interacting with the RS.

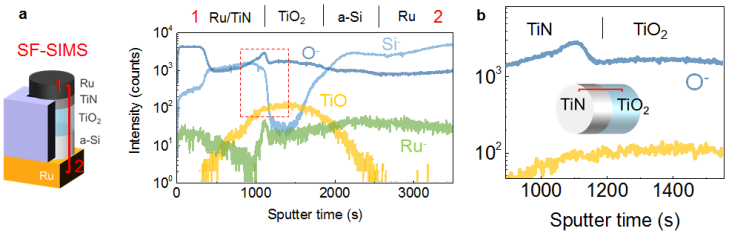

Fig. 16 SF-SIMS depth profiles recorded in the negative ion detection mode using a Bi^{1+} beam at 30 keV energy for analysis and a Cs^+ beam at 250 eV energy for sputtering, in order to obtain the O and Ti-O cluster profiles. The data is acquired on a 18 x 4 µm^2 area patterned only with the structure under study (Fig. 10a). (a) All the layers of the stack are visible in the profile, note the TiO cluster to locate the TE and BE. (b) Detailed view of the TiN/TiO_2 interface (dashed red box) reveals high concentration of oxygen likely introduced by the scavenging properties of TiN in contact with TiO_2.

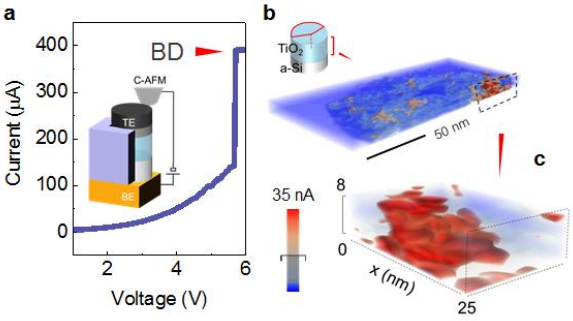

Fig. 18 (a) I-V characteristic of tip-induced BD during cycling. (b) Tomography observation of a single highly conductive spot appearing after the BD.

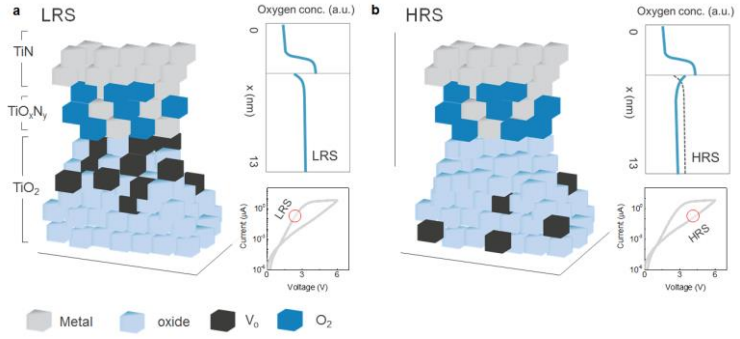

Fig. 17 Schematic of the RS model and associated oxygen profiles for the two resistance states. (a) The LRS induced by the local depletion of oxygen in proximity of the TiN/TiO_2 interface, and (b) the HRS that is characterized by the accumulation of oxygen leading to the formation of a larger tunneling barrier for transport.